Marine Structures 84 (2022) 103233

Contents lists available at ScienceDirect

Marine Structures

journal homepage: www.elsevier.com/locate/marstruc

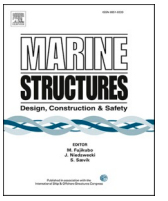

# Pressure-dependent plasticity models with convex yield loci for explicit ice crushing simulations

Mojtaba Mokhtari *, Ekaterina Kim, Jørgen Amdahl

*Centre for Autonomous Marine Operations and Systems (AMOS), Department of Marine Technology, Norwegian University of Science and Technology (NTNU), Norway*

ARTICLE INFO

*Keywords:*
Ice crushing simulations
Material modelling
Plasticity
Constitutive law
FEM

ABSTRACT

Despite the viscous behaviour of crushed ice, plasticity models have been widely used for numerical modelling of 'design-ice' in damage assessment applications for several reasons outlined herein. The Crushable Foam (CF) model and an in-house elastic-plastic VUMAT subroutine – initially developed by Liu et al. (2011) based upon Tsai-Wu yield surface – are commonly adopted to simulate glacial and freshwater ice impact loads as they are proposed to outperform the other plasticity models. Nevertheless, the similarities, differences, advantages, and limitations of the two models relative to each other are unclear. This study systematically compares these plasticity models both theoretically, in terms of their constitutive laws, and numerically in eight single-element tests and 28 different simulations of a physical cone crushing test in a laboratory scale. The effects of element size, mesh configuration, and failure parameters are also discussed. The CF plastic behaviour was defined with the Abaqus built-in CF model. The VUMAT includes a failure strain function and a cut-off pressure as failure criteria. These failure criteria were also added to the Abaqus built-in CF model using a Fortran VUSDFLD subroutine. Despite their identical yield loci, the two plasticity models were found to produce notably different results. Most importantly, the CF model, unlike the VUMAT, failed to simulate the confining pressure while it is conceivably the most used material model in the literature for ice crushing simulations. Details are discussed.

## 1. Introduction

Climate change has expediated the melting rate of large glaciers in recent decades, which may have given rise to a greater number of glacial ice features in the Arctic and Antarctic waters. Human activities like shipping, commercial fisheries, tourism, and natural resource exploration have been also increasing in the icy waters. As a result, the probability of collision between marine structures and large floating ice masses is on the rise [1]. During an ice-structure impact, large local pressures may be imposed on the collided structure, which in turn could cause failure of the structure due to large plastic deformations and/or brittle/ductile fracture.

In ice-structure collision studies, numerical methods are usually adopted to simulate the ice-structure interactions and the associated structural damage. Nevertheless, there is still no universal or widely accepted material model for crushing ice because of its exceptionally complex behaviour which is dependent on many parameters that are associated with uncertainties. These complexities have led some researchers to develop idealized material models for ice or so-called 'design-ice'. The term 'design-ice' implies that the

* Corresponding author.
*E-mail address:* mojtaba.mokhtari@ntnu.no (M. Mokhtari).

https://doi.org/10.1016/j.marstruc.2022.103233
Received 29 December 2021; Received in revised form 21 March 2022; Accepted 15 April 2022
Available online 3 May 2022

material model may not capture all the physics of crushing ice, but it is computationally efficient and can produce representative ice load intensities for damage assessment or design purposes. Although ice is shown to be a viscoelastic material with large creep strains when damaged [2–11], the most common practice to model the inelastic deformations of ice is using plastic rheology.

There are multiple reasons as to why elastic-plastic models have been widely used for design-ice instead of viscoelastic models. The most important reason could be that the plasticity models are relatively simple to work with and to calibrate for different applications. In comparison with the plasticity models, the viscoelastic models often have more material parameters leading to tedious calibration processes. In addition, the viscoelastic models may be found not fully developed for practical damage assessment applications. In the open literature, for instance, the viscoelastic models have not been used for simulating glacial or freshwater ice collisions with engineering-scale deformable steel structures. Furthermore, the better computational efficiency of the elastic-plastic models compared to the complicated viscoelastic models is another important factor. Besides, ship-ice collisions usually cause strain rates in the ice domain far greater than the 'ductile-to-brittle' transition strain rate, $10^{-4}$–$10^{-3}$ $s^{-1}$ (Fig. 1). According to Schulson [12], the 'ductile-to-brittle' transition is essentially the transition from viscous to plastic deformation. Consequently, users of the plasticity models often argue that the viscous behaviour can be neglected because the ice behaviour at high strain rates is brittle. Most importantly, unlike the viscoelastic models developed for ice-crushing, most of the plasticity models that have been used for modelling design-ice (e.g., Mohr-Coulomb, Drucker-Prager, Crushable Foam) are built-in and readily available in commercial numerical codes such as Abaqus and LS-Dyna.

In 1983, Cammaert et al. [13] outlined a framework for 3D modelling of iceberg-structure impacts including the iceberg plastic deformation, the structure elastic-plastic response, the platform excursions and the mooring system flexibility. The first implementation of fully-coupled ice-structure interaction using a plasticity material model for ice can be traced back to Kim and Kedward [14,15]. They adopted a simple built-in DYNA3D elastic-plastic model to simulate hail ice impact. The elastic-plastic material model with a non-iterative plasticity solver was defined with elastic shear modulus, yield strength, hardening modulus, bulk modulus, a constant plastic failure strain of 0.35, and a constant failure pressure of −4 MPa. In this model, the element loses its ability to carry tension and the deviatoric stresses are set to zero (i.e., the material behaves like a fluid) when the failure criteria are reached [16].

In 2006, Gagnon and Derradji [17] simulated bergy-bit collisions with the CCGS Terry Fox icebreaker using the built-in CF material model in LS-Dyna. They introduced a strain hardening behaviour for ice governed by a volumetric stress-strain curve (Fig. 2). According to this curve, when the pressure in an ice element reaches 0.1 MPa, the element undergoes non-recoverable deformation without strain hardening (i.e., pressure remains constant while the strain is increasing) until the volumetric strain is equal to 0.065. The magnitude of 0.1 MPa was found through trial and error. For volumetric strains above 0.065, the pressure increases linearly with the volumetric strain having a slope of 4.7 GPa which is about half the ice elastic modulus used in the model (9 GPa) [17,18]. In 2007, Gagnon [18] used the same material model to simulate a heavy impactor colliding with growlers. They reported that the simulation results do not support the assumption of a dependence of the nominal pressure on the nominal contact area. The material model alone could not simulate the sawtooth load pattern, typical to ice crushing and indentation tests. Therefore, Gagnon suggested a manual discretization of the ice domain to create numerous material layers. Each layer was occupied by two overlapped facets. One of the facets had a high yield stress property, and the other one was assigned a low yield stress property (Fig. 2) to model the high and low pressure zones that would enable artificial simulation of the spalling effect [19,20]. It is not clear how the number and the thickness of the layers should be determined for different crushing scenarios (e.g., different ice geometries and ice types).

Kim et al. [21–23] also employed the CF material model with a similar modelling approach to that of Gagnon [17,18]. However, instead of dividing the ice domain into numerous high strength and low strength layers, they partitioned the ice mass into two different

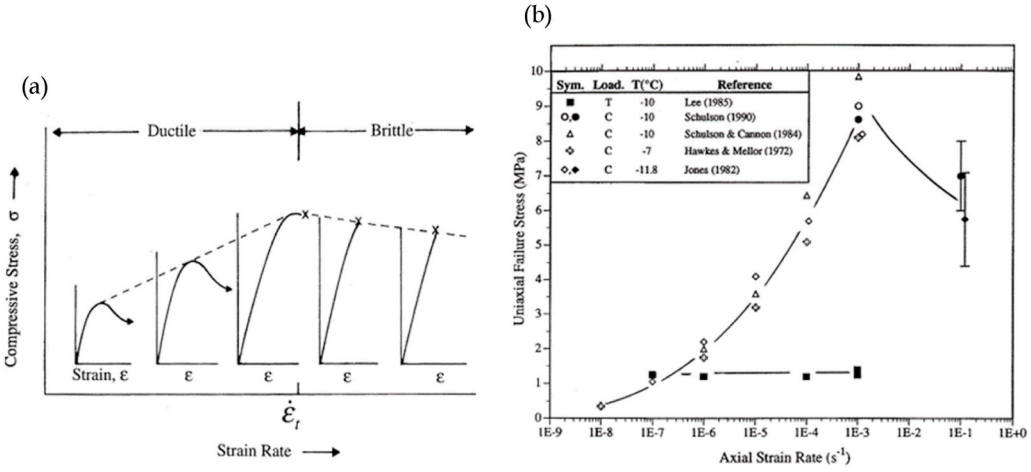


**Fig. 1.** (a) Schematic representation of the strain rate effect on the compressive stress-strain behaviour of ice. Strain hardening, followed by strain-softening, strain-rate hardening and macroscopically ductile behaviour occur at lower rates ($\dot{\varepsilon} < \dot{\varepsilon}_t$). At higher rates, strain-rate softening and macroscopically brittle behaviour are observed [12]. (b) Strain rate effect on the uniaxial compressive strength (C, upper curve) of equiaxed and randomly oriented polycrystals of ice at ~−10 °C. The tensile strength (T) from Lee (1985) is shown for comparison [12].

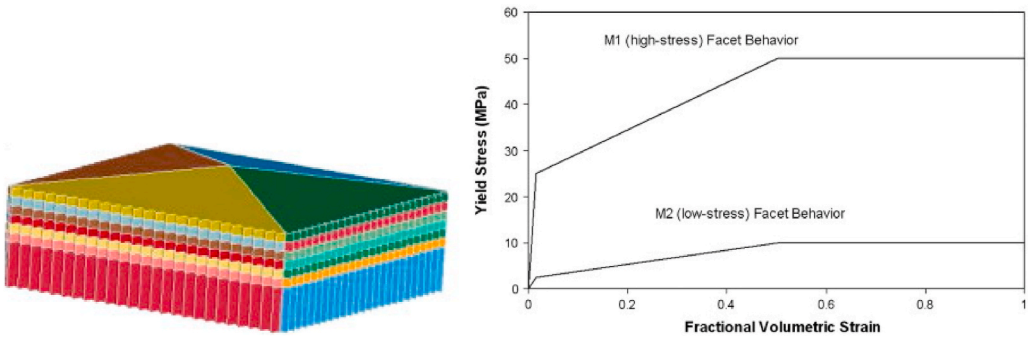


**Fig. 2.** Gagnon's multi-layer modelling approach with two different volumetric hardening curves for each layer [20].

domains to reflect a High Pressure Zone (HPZ) at the centre of the contact region and a Low Pressure Zone (LPZ) at the outer part as displayed in Fig. 3. Although modelling two different strength zones in the ice domain is simpler than dividing the ice into numerous layers, it is not still clear how one can configure the partitions for HPZ and LPZ in different crushing scenarios with different ice geometries, types, temperature, etc.

Several other studies utilized the CF plasticity to model the ice crushing process (e.g., Refs. [24–30]). Han et al. [30] reported that the CF plasticity model is generally more suitable for ice crushing simulation compared to Drucker-Prager and Mohr-Coulomb. This conclusion was made by comparing experimental force-displacement plots from cone ice indentation tests with the numerical results. Numerical force-displacement curves were produced by finite element models of the cone ice composed of multiple layers, somewhat similar to Gagnon's multi-layer approach, but with different fracture energies for the damage evolution of each layer.

In 2011, Liu et al. [1] developed an elastic-plastic material model based upon Tsai-Wu yield surface with a user-defined failure model. Three different numerical studies were conducted to investigate the performance of the material model. First, an iceberg collision with a rigid wall was simulated which, for the given set of input parameters to the models, produced a 'contact pressure - contact area' (*P-A*) curve correlating closely with the semi-empirical ISO-ALIE curve [31] ($P = 7.4A^{-0.7}$). Then, Pond Inlet test was simulated and a good agreement with the experimental *P-A* curves was achieved. Finally, a full-scale ship bow-iceberg head-on collision was simulated using the validated material model. This ice model was initially scripted in a VUMAT for LS-Dyna, and later other versions of it were developed for both LS-Dyna and Abaqus used in several studies (e.g., Refs. [32–37]). Details of the plasticity constitutive law and the failure model are given in the next section.

As mentioned earlier, most studies that have employed the CF plasticity to define the plastic behaviour of ice have divided the ice mass into different strength zones with different hardening properties. These manual interventions suggest that the CF material model (i.e., constitutive stress-strain relationships with material parameters) is supposedly missing an important physical property of crushing ice which needs to be added through the manual discretization (i.e., the manual assignment of HPZ and LPZ properties to the ice domain). To address this hypothesis in the present study, the ice mass is modelled without the manual discretization technique. In other words, the ice domain includes only one material model (i.e., either Crushable Foam or VUMAT) with only one set of input values for the material parameters. The results from the CF model and the VUMAT will be compared relative to each other and to those from physical tests. The similarities and differences between the constitutive laws of the CF plasticity and the plasticity rule in the VUMAT are also scrutinized. Furthermore, these two plasticity models are compared in a single-element study with different loading scenarios (in total eight single-element tests). Single-element tests showcase the material behaviour with more clarity, including the effects of using the two plasticity models on the stress, strain, and most importantly, the hydrostatic pressure.

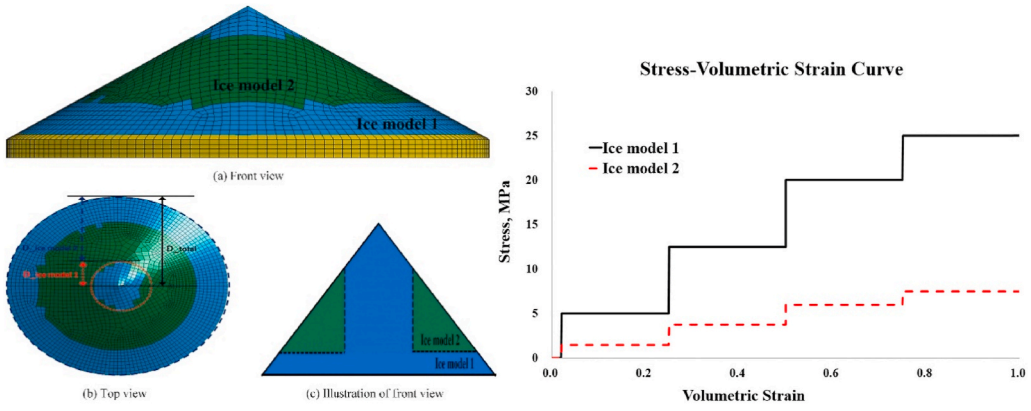


**Fig. 3.** Kim et al. [23] two-zone modelling approach with a different volumetric hardening curve for each zone.

## 2. Constitutive laws

### 2.1. VUMAT

The VUMAT defines ice as an elastic-perfectly plastic material with a pressure-dependent convex yield surface. The model constitutive equations, assumptions and implementation have not been discussed earlier in detail, and thus are provided herein.

Derradji-Aouat [38] proposed a yield surface based upon the empirical data from triaxial experiments with iceberg and glacier ice carried out by Gagnon and Gammon [39]. This yield surface is an elliptical envelope in $p$-$\tau$ space defined by

$$\left(\frac{\tau-\eta}{\tau_{\max}}\right)^2+\left(\frac{p-\xi}{p_c}\right)^2=1 \tag{1}$$

where $\eta$, $\tau_{\max}$, $\xi$, and $p_c$ are constants, $p=-\frac{1}{3}\mathrm{tr}\ (\boldsymbol{\sigma})$ is the hydrostatic pressure (positive for compression), $\boldsymbol{\sigma}=\sigma_{ij}e_i\otimes e_j$ is the Cauchy stress tensor, $e_1,\ldots,e_3$ are orthonormal vectors, $\tau=\sqrt{\frac{\mathbf{s}:\mathbf{s}}{3}}$ is the octahedral stress, $\mathbf{s}=s_{ij}e_i\otimes e_j=\boldsymbol{\sigma}+p\mathbf{I}$ is the deviatoric stress tensor. For $\eta=0$, assuming an isotropic material condition, the yield surface proposed by Derradji-Aouat [38] would be the same as the so-called Tsai-Wu yield surface (Fig. 4) [40],

$$f(p,q)=q-\sqrt{a_0+a_1p+a_2p^2} \tag{2}$$

where $q=\sqrt{\frac{3}{2}\mathbf{s}:\mathbf{s}}$ is the von Mises stress, and $a_0$, $a_1$, and $a_2$ are material constants obtained from triaxial compression tests.

In order to make the implementation convenient, the Tsai-Wu yield surface is rewritten in $p-J_2$ space with updated material constants as

$$\varphi(p,J_2)=J_2-\left(a_0^{'}+a_1^{'}p+a_2^{'}p^2\right) \tag{3}$$

where $J_2=\frac{q^2}{3}$ is the second invariant of the deviatoric stress tensor.

Temperature and loading rate (strain rate) can affect the material constants in most collision scenarios. With temperature and strain rate effects included, Eq. (3) can be expressed as

$$\varphi^*(p,J_2,T,\dot{\varepsilon}_v)=J_2-a_0^*(T,\dot{\varepsilon}_v)+a_1^*(T,\dot{\varepsilon}_v)p+a_2^*(T,\dot{\varepsilon}_v)p^2 \tag{4}$$

where $T$ is temperature and $\dot{\varepsilon}_v=\frac{d\varepsilon_v}{dt}$ is the volumetric strain rate depending on element size and sound speed. The original model developed by Liu et al. [1] does not account for the effects of temperature and strain rate. Therefore, it is up to the user to recalibrate the material parameters for different loading rates and ice temperatures. To compare the VUMAT with the CF material model under equal conditions, the original model without temperate and strain-rate dependency has been used in this study. It should be noted that the CF material model used in the literature for ice modelling is also temperature and strain-rate independent [17–20,27] [21-23].

Voigt notation was used to map symmetric second-order tensors and fourth-order tensors with minor symmetry into a vector and matrix space to perform the algebraic operations in the VUMAT. Using Voigt notations, 6-dimensional stress and strain vectors, $\widetilde{\boldsymbol{\sigma}}$ and $\widetilde{\boldsymbol{\varepsilon}}$, are

$$\widetilde{\boldsymbol{\sigma}}=(\sigma_1,\sigma_2,\sigma_3,\sigma_4,\sigma_5,\sigma_6)^T\equiv(\sigma_{11},\sigma_{22},\sigma_{33},\sigma_{12},\sigma_{23},\sigma_{31})^T \tag{5}$$

$$\widetilde{\boldsymbol{\varepsilon}}=(\varepsilon_1,\varepsilon_2,\varepsilon_3,\varepsilon_4,\varepsilon_5,\varepsilon_6)^T\equiv(\varepsilon_{11},\varepsilon_{22},\varepsilon_{33},2\varepsilon_{12},2\varepsilon_{23},2\varepsilon_{31})^T \tag{6}$$

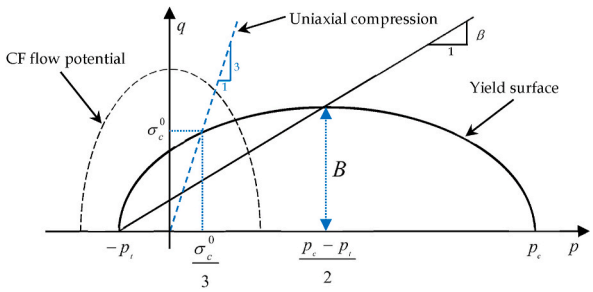


**Fig. 4.** Yield surface and flow potential in $p$–$q$ space for the VUMAT and the CF model.

The stress-strain relationship in the Voigt form can be written as

$$\dot{\tilde{\boldsymbol{\sigma}}} = \tilde{\tilde{\mathbf{C}}}^{e} \left(\dot{\tilde{\boldsymbol{\varepsilon}}} - \dot{\tilde{\boldsymbol{\varepsilon}}}^{p}\right) \tag{7}$$

where $\dot{\tilde{\boldsymbol{\sigma}}}$ is stress rate, $\dot{\tilde{\boldsymbol{\varepsilon}}} = \dot{\tilde{\boldsymbol{\varepsilon}}}^{e} + \dot{\tilde{\boldsymbol{\varepsilon}}}^{p}$ is total stain rate, $\dot{\tilde{\boldsymbol{\varepsilon}}}^{e}$ is elastic strain rate, $\dot{\tilde{\boldsymbol{\varepsilon}}}^{p}$ is plastic strain rate, and $\tilde{\tilde{\mathbf{C}}}^{e}$ is the Voigt representation of the elastic stiffness tensor, $\mathbb{C}^{e} = C_{ijkl}\, e_i \otimes e_j \otimes e_k \otimes e_l$, that is a fourth order tensor with minor symmetry (i.e., $C_{ijkl} = C_{jikl} = C_{ijlk} = C_{jilk}$) [41]. Using Lamé parameters, the elastic stiffness matrix, $\tilde{\tilde{\mathbf{C}}}^{e}$, is expressed as

$$\tilde{\tilde{\mathbf{C}}}^{e} = \begin{bmatrix} 2\mu+\lambda & \lambda & \lambda & 0 & 0 & 0 \\ \lambda & 2\mu+\lambda & \lambda & 0 & 0 & 0 \\ \lambda & \lambda & 2\mu+\lambda & 0 & 0 & 0 \\ 0 & 0 & 0 & \mu & 0 & 0 \\ 0 & 0 & 0 & 0 & \mu & 0 \\ 0 & 0 & 0 & 0 & 0 & \mu \end{bmatrix};\ \lambda = \frac{E\nu}{(1+\nu)(1-2\nu)};\ \mu = \frac{E}{2(1+\nu)} \tag{8}$$

If the normality rule is enforced, the plastic strain rate for the associated flow rule is found from

$$\dot{\tilde{\boldsymbol{\varepsilon}}}^{p} = \dot{\gamma}\boldsymbol{\alpha}\ ;\ \boldsymbol{\alpha} = \frac{\partial \Phi}{\partial \tilde{\boldsymbol{\sigma}}} = \frac{\partial \Phi}{\partial J_2}\frac{\partial J_2}{\partial \tilde{\boldsymbol{\sigma}}} + \frac{\partial \Phi}{\partial p}\frac{\partial p}{\partial \tilde{\boldsymbol{\sigma}}} \tag{9a; 9b}$$

where $\dot{\gamma}$ is the consistency parameter also known as the plastic multiplier, $\Phi$ is the plastic potential function (Eq. (3)), and $\boldsymbol{\alpha}$ is the flow direction. The consistency parameter must satisfy the loading-unloading or Kuhn-Tucker conditions,

$$\dot{\gamma} \geq 0,\ \Phi \leq 0\ ,\ \dot{\gamma}\Phi = 0 \tag{10}$$

The rate constitutive equations are integrated incrementally as follows [42].

$$\tilde{\boldsymbol{\varepsilon}}^{p} = \sum_{1}^{n+1} \Delta\tilde{\boldsymbol{\varepsilon}}_i^{p};\ \tilde{\boldsymbol{\varepsilon}}_{n+1}^{p} = \tilde{\boldsymbol{\varepsilon}}_{n}^{p} + \Delta\gamma_{n+1}\boldsymbol{\alpha}_{n+1};\ \Delta\gamma_{n+1} = \dot{\gamma}_{n+1}\Delta t_{n+1} \tag{11a; 11b; 11c}$$

$$\tilde{\boldsymbol{\sigma}} = \sum_{1}^{n+1} \Delta\tilde{\boldsymbol{\sigma}}_i;\ \tilde{\boldsymbol{\sigma}}_{n+1} = \tilde{\tilde{\mathbf{C}}}^{e}\left(\tilde{\boldsymbol{\varepsilon}}_{n+1} - \tilde{\boldsymbol{\varepsilon}}_{n+1}^{p}\right) \tag{12a; 12b}$$

$$\tilde{\boldsymbol{\varepsilon}}_{n+1} = \tilde{\boldsymbol{\varepsilon}}_{n} + \Delta\tilde{\boldsymbol{\varepsilon}}_{n+1};\ \Delta\tilde{\boldsymbol{\varepsilon}}_{n+1} = \dot{\tilde{\boldsymbol{\varepsilon}}}_{n+1}\Delta t_{n+1} \tag{13a; 13b}$$

where $\Delta t_{n+1} = t_{n+1} - t_n$ is the time step size. At the beginning of each time step an elastic predictor, so-called trial stress $\tilde{\boldsymbol{\sigma}}_{n+1}^{tr}$, is first calculated by summing the back stress and the new stress increment calculated from the elastic equations

$$\tilde{\boldsymbol{\sigma}}_{n+1}^{tr} = \tilde{\boldsymbol{\sigma}}_{n} + \tilde{\tilde{\mathbf{C}}}^{e}\,\Delta\tilde{\boldsymbol{\varepsilon}}_{n+1} \tag{14}$$

Then, if the material stress exceeds yielding, the trial stress is mapped back on the yield surface and the strain is updated using the Cutting Plane Algorithm (CPA) as the return mapping algorithm. To judge if the material is yielding, a conditional statement of the yield function is defined as

$$\varphi(p^{tr}, J_2{}^{tr}) = J_2{}^{tr} - \left(a_0^{'} + a_1^{'}p^{tr} + a_2^{'}(p^{tr})^2\right) \leq 0 \tag{15}$$

If the condition is true, the trial stress is returned as the actual stress and no mapping to the yield surface is required. Otherwise, the trial stress will be returned to the yield surface using CPA with Newton–Raphson iterations. By rewriting Eq. (12b) in the Newton–Raphson iteration scheme, the sequential stress in each iteration is

$$\tilde{\boldsymbol{\sigma}}_{n+1}^{(k+1)} = \tilde{\tilde{\mathbf{C}}}^{e}\left(\tilde{\boldsymbol{\varepsilon}}_{n+1} - \tilde{\boldsymbol{\varepsilon}}_{n+1}^{p(k+1)}\right) \tag{16}$$

where $\tilde{\boldsymbol{\varepsilon}}_{n+1}^{p(k+1)}$ can be found from

$$\tilde{\boldsymbol{\varepsilon}}_{n+1}^{p(k+1)} = \tilde{\boldsymbol{\varepsilon}}_{n+1}^{p(k)} + \Delta\gamma_{n+1}^{(k)}\boldsymbol{\alpha}_{n+1}^{(k)} \tag{17}$$

Having Eq. (17) substituted in Eq. (16) and knowing that

$$\tilde{\boldsymbol{\sigma}}_{n+1}^{(k)} = \tilde{\boldsymbol{\sigma}}_{n+1}^{tr} = \tilde{\tilde{\mathbf{C}}}^{e}\left(\tilde{\boldsymbol{\varepsilon}}_{n+1} - \tilde{\boldsymbol{\varepsilon}}_{n+1}^{p(k)}\right) \tag{18}$$

we have

$$\widetilde{\boldsymbol{\sigma}}_{n+1}^{(k+1)} = \widetilde{\boldsymbol{\sigma}}_{n+1}^{(k)} - \Delta\gamma_{n+1}^{(k)} \widetilde{\mathbf{C}}^{e} \boldsymbol{\alpha}_{n+1}^{(k)};\ \Delta\widetilde{\boldsymbol{\sigma}}_{n+1}^{(k)} = -\Delta\gamma_{n+1}^{(k)} \widetilde{\mathbf{C}}^{e} \boldsymbol{\alpha}_{n+1}^{(k)} \tag{19a; 19b}$$

Considering a perfectly plastic condition, $\Phi$ is linearized around the current value of stress, $\widetilde{\boldsymbol{\sigma}}^{(k)}$, as

$$\left(\Phi^{(k+1)} - \Phi^{(k)}\right)_{n+1} = \left(\frac{\partial\Phi}{\partial J_2}\frac{\partial J_2}{\partial\widetilde{\boldsymbol{\sigma}}} + \frac{\partial\Phi}{\partial p}\frac{\partial p}{\partial\widetilde{\boldsymbol{\sigma}}}\right)_{n+1}^{(k)} \left(\widetilde{\boldsymbol{\sigma}}^{(k+1)} - \widetilde{\boldsymbol{\sigma}}^{(k)}\right)_{n+1} = 0 \tag{20}$$

By substituting $\left(\widetilde{\boldsymbol{\sigma}}^{(k+1)} - \widetilde{\boldsymbol{\sigma}}^{(k)}\right)_{n+1}$ from Eq. (19b) with $\boldsymbol{\alpha}$ given in Eq. (9b), and setting $\Phi^{(k+1)} = 0$, the plastic multiplier is found

$$\Delta\gamma_{n+1}^{(k)} = \frac{\Phi_{n+1}^{(k)}}{\left(\left(\frac{\partial\Phi}{\partial J_2}\frac{\partial J_2}{\partial\widetilde{\boldsymbol{\sigma}}} + \frac{\partial\Phi}{\partial p}\frac{\partial p}{\partial\widetilde{\boldsymbol{\sigma}}}\right)_{n+1}^{(k)}\right)^{T} \widetilde{\mathbf{C}}^{e} \left(\frac{\partial\Phi}{\partial J_2}\frac{\partial J_2}{\partial\widetilde{\boldsymbol{\sigma}}} + \frac{\partial\Phi}{\partial p}\frac{\partial p}{\partial\widetilde{\boldsymbol{\sigma}}}\right)_{n+1}^{(k)}} \tag{21}$$

With the updated plastic multiplier, $\Delta\gamma_{n+1}^{(k)}$, the stress and strain increments are calculated from Eq. (17) and Eq. (19b). The iterations continue until a convergence criterion is met. In other words, the trial stress is deemed returned on the yield surface when a certain number of iterations is reached (e.g., 200 iterations) or if $\Phi^{(k)} \leq \delta$, where $\delta$ is the convergence tolerance (e.g., $10^{-9}$). Further information about the return mapping algorithm can be found in Refs. [42,43].

### 2.2. Crushable foam

The built-in Crushable Foam plasticity model in Abaqus [44] was employed for the benchmark study. This plasticity model is also based upon the Tsai-Wu yield surface (Fig. 4), discussed in the previous section. However, it is formulated differently as

$$\psi(p,q) = \sqrt{q^2 + \beta^2(p - p_0)^2} - B = 0 \tag{22}$$

where $B = \beta A = \beta\left(\frac{p_c + p_t}{2}\right)$ is the vertical semiaxis of the yield ellipse (along the $q$-axis in Fig. 4), $\beta = \frac{B}{A}$ is the shape factor of the yield ellipse defining the relative magnitude of the axes, $A$ is the horizontal semiaxis of the yield ellipse (along the $p$-axis), $p_0 = \frac{p_c - p_t}{2}$ is the yield ellipse centre on the $p$-axis, and $p_t$ and $p_c$ are the material strength in hydrostatic tension and hydrostatic compression, respectively ($p_c$ is always positive). The shape factor,$\beta$, is computed using the initial yield stress in uniaxial compression, $\sigma_c^0$, the yield strength in hydrostatic compression, $p_c$, and the yield strength in hydrostatic tension, $p_t$ [44], as follows

$$\beta = \frac{3k}{\sqrt{(3k_t + k)(3 - k)}};\ k = \frac{\sigma_c^0}{p_c};\ k_t = \frac{p_t}{p_c} \tag{23a; 23b; 23c}$$

For a valid yield surface, the strength ratios must meet the following conditions

$$0 < k < 3 \quad \text{and} \quad k_t \geq 0 \tag{24}$$

Plastic deformation is determined using a non-associated flow rule. In tensor form, the plastic strain rate is found from

$$\dot{\boldsymbol{\varepsilon}}^{p} = \dot{\bar{\varepsilon}}^{p}\frac{\partial G}{\partial\boldsymbol{\sigma}} \tag{25}$$

where $G$ is the flow potential defined as

$$G = g(q,p) = \sqrt{q^2 + \frac{9}{2}p^2} \tag{26}$$

and $\dot{\bar{\boldsymbol{\varepsilon}}}^{p}$ is the equivalent strain rate found from

$$\dot{\bar{\varepsilon}}^{p} = \frac{\boldsymbol{\sigma} : \dot{\boldsymbol{\varepsilon}}^{p}}{G} \tag{27}$$

The flow potential is estimated from simple laboratory experiments on foam materials which suggest loading in any principal direction causes insignificant deformation in the other directions. In other words, plastic Poisson's ratio, $\nu_p$, is zero [20,44]. Therefore, the equivalent plastic strain rate is related to the rate of axial plastic strain, $\dot{\varepsilon}_{axial}^{p}$, in uniaxial compression tests by

$$\dot{\bar{\boldsymbol{\varepsilon}}}^{p} = \sqrt{\frac{2}{3}}\dot{\boldsymbol{\varepsilon}}_{axial}^{p} \tag{28}$$

No information about the return mapping algorithm used for the Crushable Foam plasticity model is provided in the Abaqus user's

manual [44]. It is worth noting that the built-in Crushable Foam model in LS-Dyna has essentially the same constitutive law as that in Abaqus and returns a zero plastic Poisson's ratio [45].

## 3. Relationship between CF and VUMAT material constants

In order to use the built-in CF model in Abaqus, one needs to provide the values of $k$ and $k_t$, and $\sigma_c^0$ as input. In the literature, however, the yield surface is usually defined by Eq. (2) or Eq. (3) using the material constants $(a_0, a_1, a_2)$ or $(a_0', a_1', a_2')$. The relationships between $k$ and $k_t$ and $a_0'$, $a_1'$, $a_2'$ are therefore derived herein. First, the roots of the parabolic function in Eq. (3) are found as

$$p_c, p_t = \frac{-a_1' \pm \sqrt{a_1'^2 - 4a_0'a_2'}}{2a_2'} \tag{29}$$

If the yield surface given in Eq. (3) is mapped in $p$-$q$ space (Fig. 4), it intersects with the uniaxial compression line, $q = 3p$, where $q = \sigma_c^0$. Substituting $J_2 = \frac{(\sigma_c^0)^2}{3}$ and $p = \frac{\sigma_c^0}{3}$ in Eq. (3) gives

$$\sigma_c^0 = \sqrt{3\left(a_0' + a_1'\frac{\sigma_c^0}{3} + a_2'\left(\frac{\sigma_c^0}{3}\right)^2\right)} \tag{30}$$

Solving the above equation yields

$$\sigma_c^0 = 3\frac{a_1' + \sqrt{a_1'^2 - 4(a_2' - 3)a_0'}}{2(3 - a_2')} \tag{31}$$

By substituting Eqs. (29) and (31) in Eq. (23), the CF model constants are found as

$$k_t = \frac{a_1' - \sqrt{a_1'^2 - 4a_0'a_2'}}{a_1' + \sqrt{a_1'^2 - 4a_0'a_2'}} \tag{32}$$

$$k = 3\frac{a_2'\left(a_1' + \sqrt{a_1'^2 - 4(a_2' - 3)a_0'}\right)}{(a_2' - 3)\left(a_1' + \sqrt{a_1'^2 - 4a_0'a_2'}\right)} \tag{33}$$

## 4. Failure model

A general form of the failure model proposed by Liu et al. [1] is used herein for both the VUMAT and the CF model. The original failure model includes a cut-off pressure, $p_{cut}$, and an empirical failure strain defined by an effective plastic strain, $\bar{\varepsilon}^p$, and the hydrostatic pressure, $p$, as

$$\varepsilon_f = \varepsilon_0 + \left(\frac{p}{p_c} - 0.5\right)^2 \tag{34}$$

$$\bar{\varepsilon}^p = \sqrt{\frac{2}{3}\mathbf{e}^p : \mathbf{e}^p} \tag{35}$$

where $\varepsilon_f$ is the failure strain, $\varepsilon_0$, is the initial failure strain found from lab test data, $\mathbf{e}^p = \boldsymbol{\varepsilon}^p - \varepsilon_m^p\mathbf{I}$ is the deviatoric plastic strain, and $\varepsilon_m^p = \frac{1}{3}tr(\boldsymbol{\varepsilon}^p)$ is the mean plastic strain. Eq. (34) is derived empirically from trial and error simulations. It means that it may not be valid for conditions other than those under which the formulation is derived. Therefore, a more general form of Eq. (34) is used in the current study defined as

$$\varepsilon_f = \varepsilon_0 + \left(\frac{p}{M\ p_c} - \frac{N}{M}\right)^2 \tag{36}$$

where $M$ and $N$ are constants to be calibrated. If in an element $\bar{\varepsilon}^p > \varepsilon_f$ or $p < p_{cut}$, erosion is activated meaning that the element is deleted from subsequent analysis. The nodes of eroded elements act as free-flying point masses that experience contact with the active contact faces and transfer momentum [44].

## 5. Numerical modelling

Numerical analyses in this study were performed using the finite element code Abaqus 2019. Plastic behaviours simulated by the

VUMAT and the CF model were compared in two different modelling frameworks. First, a 'single-element test' model with eight different load cases was developed to validate the material laws and the failure model. The single-element test also allowed for a fundamental comparison of the VUMAT and the CF model. To confirm the findings from the single-element test, an experimental cone ice crushing test was modelled using the VUMAT and the CF model.

### 5.1. Single-element test

A unit cube (area of each face equal to 1 $mm^2$) test was set up, meshed with a single, linear, hexahedral, reduced integration (C3D8R) element. In order to achieve cube deformations that truly correspond to uniaxial loading conditions, appropriate symmetry conditions were applied on three faces as shown in Fig. 5 (three symmetry planes XY, XZ and YZ). These settings are recommended by Simuleon B.V. (a partner of Dassault Systèmes Simulia Corp. that provides Abaqus software) official documents for Abaqus users [46].

Table 1 lists eight different load cases studied for each material model. In a two-step loading scenario and for six different load cases, the initial yield stresses produced by the VUMAT and the CF model were checked to see whether they occur on the theoretical yield surface. In each load case, the element first undergoes an initial pressure, $P_0$, which is applied in step 1 (see Fig. 6a). Then, in the second step, a uniaxial displacement, $D = 0.5$ mm, is enforced in X direction (displacement-controlled). The length of each step is 50 ms, resulting in a total time of 100 ms.

Two more cases (Case #7 and #8) were also simulated. Case#7, which evaluates the performance of the failure model was developed by adding the failure model to Case #3. Case #8 was developed to compare the confining pressure produced by each of the two plasticity models in a confined space. For this purpose, Case #7 was modified by adding two fixed planes on two sides of the element to create a confined space with rigid walls (Fig. 6b). Values of $p_t$, $p_c$ and other material parameters are given in the next section.

### 5.2. Cone ice crushing

One of the cone ice crushing tests carried out by Kim et al. [22] was simulated using the VUMAT and the CF model. The experimental setup and the corresponding finite element model are shown in Fig. 7. The experimental study included two different indenter speeds, 1 mm/s and 100 mm/s. The 100 mm/s test is used for the benchmark study herein. This is because the 1 mm/s test might incorporate some viscoelastic behaviour requiring a strain rate sensitive material model, and neither the VUMAT nor the CF model in this study is strain rate dependent. For computational efficiency, only a quarter of the cone is modelled. A preliminary study with a full model was carried out to ensure the quarter model and the full model produce very similar results.

Mesh sensitivity analysis was carried out for both the VUMAT and the CF model with five different element sizes (Fig. 8). For a proper mesh sensitivity analysis, a uniform mesh was required throughout the ice domain. Hence, the mesh was generated through a bottom-up iterative technique given that Abaqus automatic meshing generates elements with significantly different sizes, shapes and aspect ratios in the conical mesh domain. The automatic meshing can also generate poor quality elements leading to a computationally more expensive simulation. The bottom-up meshing technique provided the desired uniform mesh. However, this technique results in an uneven surface where the cone base should come in touch with the ice holder (Fig. 8). To diminish the effect of this uneven surface on the results to a negligible amount, a few extra layers of elements at the cone base were developed and all the element nodes located outside of the target ice domain were fixed to simulate the ice holder effect. This means all nodes inside the dashed box in Fig. 8 were fixed. It should be emphasized that the fixed nodes are located a significant distance from the indenter stop point and the plastic deformation zone. Therefore, the uneven fixed boundary has a negligible effect on results.

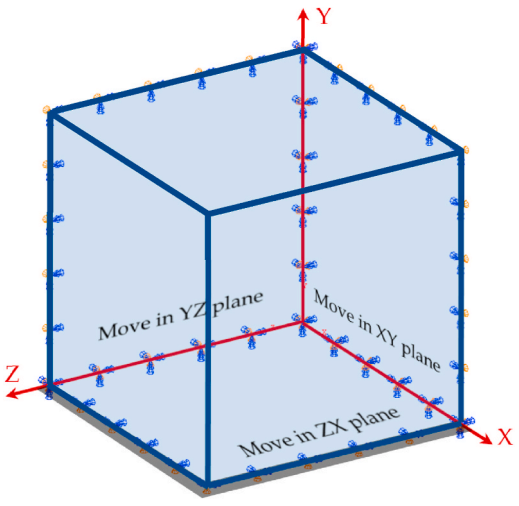


**Fig. 5.** Element boundary conditions.

**Table 1**
Load cases in the single-element study.

| Case # | Initial pressure applied in step 1, $P_0$ (MPa) | Displacement applied in step 2, $D$ (mm) | Failure model |
|---|---|---|---|
| 1 | $-p_t$ | 0.5[a] | No |
| 2 | 0 | 0.5 | No |
| 3 | 0 | −0.5 | No |
| 4 | $\frac{p_c - p_t}{2}$ | −0.5 | No |
| 5 | $\frac{3}{4}(p_c - p_t)$ | −0.5 | No |
| 6 | $p_c$ | −0.5 | No |
| 7 | 0 | −0.5 | Yes |
| 8 | 0[b] | −0.5 | Yes |

[a] Positive $D$ values indicate tensile loading.
[b] Confining pressure will be induced in step 2 by fixed rigid walls limiting transverse deformations of the element under compression.

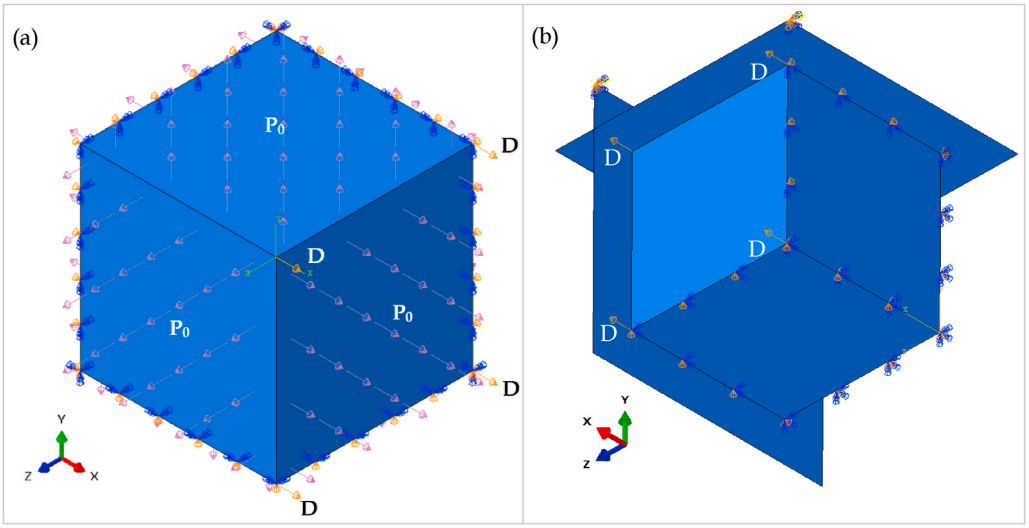


**Fig. 6.** Loading and boundary conditions for the single-element tests. (a) Cases #1 – #7. $D$ indicates displacement along X direction applied to four nodes. $P_0$ is the applied pressure load on the three free faces. (b) Case #8 with uniaxial compressive displacement, $D$, and two fixed planes to model confinement by restricting transverse deformations of the element under compressive loading.

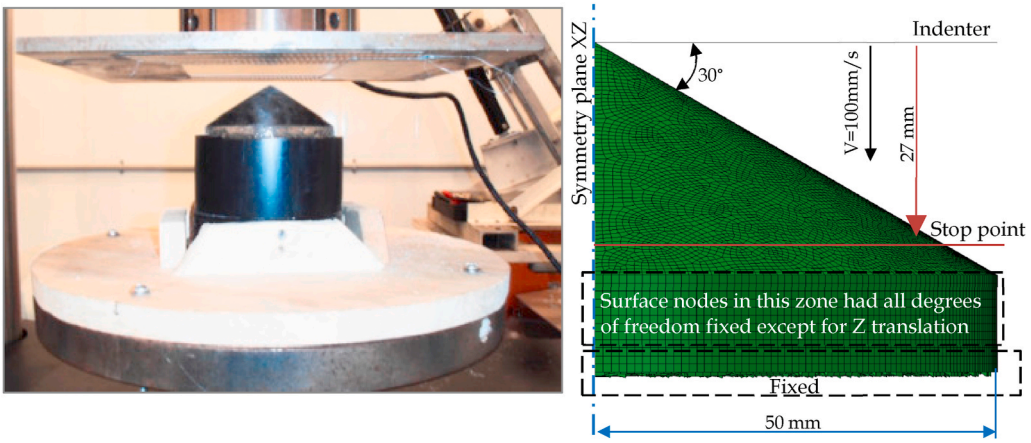


**Fig. 7.** Cone-shaped ice; left) test set-up [22]; right) finite element model (a quarter FE model was developed for computational efficiency).

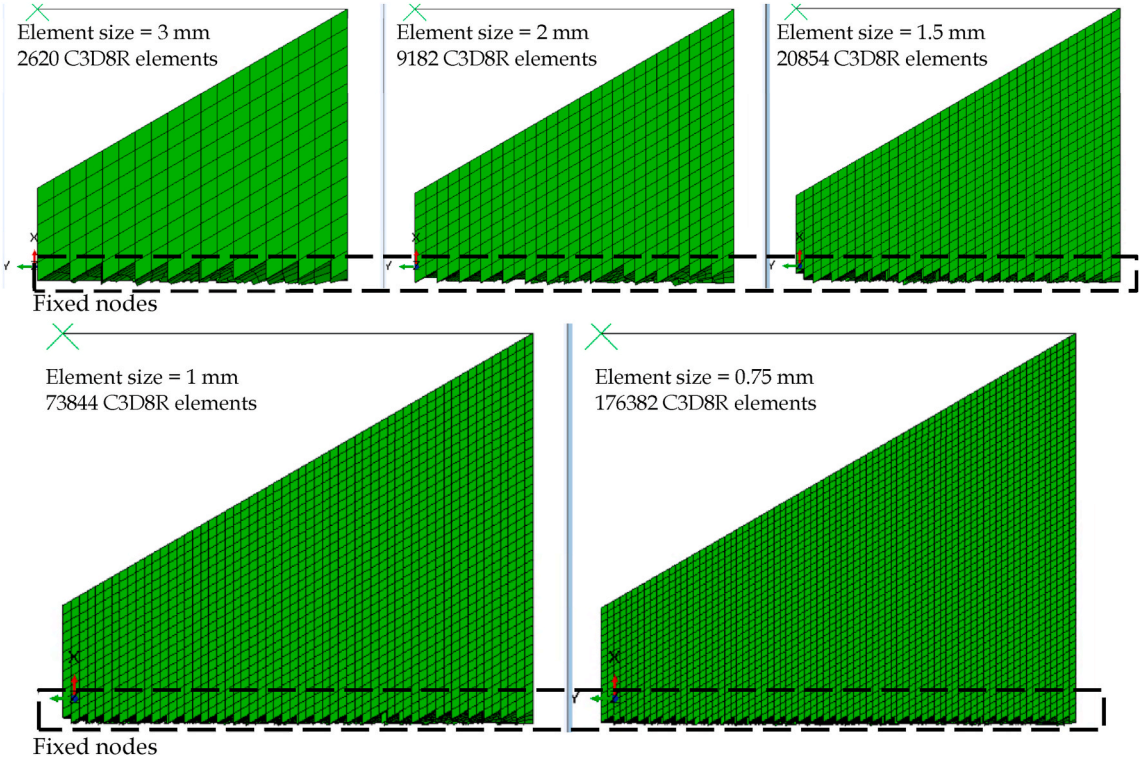


**Fig. 8.** Five different element sizes used for the mesh sensitivity analysis.

**Table 2**
Ice material parameters for the VUMAT and the CF model.

| Young's modulus, $E$ (MPa) | Elastic Poisson's ratio, $\nu_e$ | Initial density, $\rho_0$ (kg/m$^3$) | $p_c$ (MPa) | $p_t$ (MPa) |
|---|---|---|---|---|
| 9500 [1] | 0.003[a] | 900 [1] | 53.234 [1,47] | 0.293 [1,47] |
| $a_0^{'}$ (MPa$^2$) | $a_1^{'}$ (MPa) | $a_2^{'}$ | $k$ | $k_t$ |
| 2.588 [1,47] | 8.63 [1,47] | −0.163 [1,47] | 0.1691 | 0.0056 |

[a] The Poisson's ratio is from the crushable foam studies [18,22,27]. A Poisson's ratio of 0.3 was also tested. The VUMAT with elastic Poisson's ratio of 0.3 produced almost the same results. However, the CF model occasionally produced extremely "noisy" results for elastic Poisson's ratio of 0.3. To avoid the noise, the Poisson's ratio of 0.003 was eventually adopted. The noise for models with 0.3 elastic Poisson's ratio could be due to the fact that the CF model returns a zero plastic Poisson's ratio.

Table 2 lists the material input values to the finite element models of this study. Kierkegaard's values [47] listed in Ref. [1] were adopted to define the size of the yield surface. Failure strain and cut-off pressure were set to 0.01 and −2 MPa, respectively [1]. A calibration study was conducted for the failure parameters, $M$ and $N$. Six different sets of values were evaluated for $M$ and $N$. The first two sets were investigated alongside the mesh sensitivity analysis. After the proper element size was determined, the calibration study was continued using the appropriate element size. Table 3 summarizes all the cone ice crushing models developed for the mesh sensitivity and calibration studies.

## 6. Results of the finite element tests and discussion

### 6.1. Single-element test

Results from the first six load cases (i.e., Cases #1 – #6) for both material models are plotted in $p$-$q$ space in Fig. 9. Both material models have very similar initial yield points and $p$-$q$ paths to the yield points for all the load cases. In Case #4, a small noise is observed right after the yield stress is reached for the CF model.

The von Mises stress, hydrostatic pressure, equivalent plastic strain and failure strain evolution for Cases #7 and #8 are shown in Fig. 10. For these cases, $M = 1$ and $N = 0.75$ were used in the failure strain equation (Eq. (36)). According to the failure model, once the failure criterion ($p_{cut}$ or failure strain) is reached, the erosion is activated. In Cases #7 and #8, the element is under compression and thus the failure strain is the criterion that determines the element deletion. Both the VUMAT and the CF model activated erosion once

**Table 3**
Details of the cone ice crushing models.

| Material model | *M* | *N* | Element size | Model # |
|---|---|---|---|---|
| VUMAT | 1 | 0.5 | 3 | $VUMAT_{1\text{-}0.5\text{-}3}$ |
| | | | 2 | $VUMAT_{1\text{-}0.5\text{-}2}$ |
| | | | 1.5 | $VUMAT_{1\text{-}0.5\text{-}1.5}$ |
| | | | 1 | $VUMAT_{1\text{-}0.5\text{-}1}$ |
| | | | 0.75 | $VUMAT_{1\text{-}0.5\text{-}0.75}$ |
| | 1 | 0.75 | 3 | $VUMAT_{1\text{-}0.75\text{-}3}$ |
| | | | 2 | $VUMAT_{1\text{-}0.75\text{-}2}$ |
| | | | 1.5 | $VUMAT_{1\text{-}0.75\text{-}1.5}$ |
| | | | 1 | $VUMAT_{1\text{-}0.75\text{-}1}$ |
| | | | 0.75 | $VUMAT_{1\text{-}0.75\text{-}0.75}$ |
| | 1 | 0.68 | 1 | $VUMAT_{1\text{-}0.68\text{-}1}$ |
| | 0.6 | 0.5 | 1 | $VUMAT_{0.6\text{-}0.5\text{-}1}$ |
| | 0.5 | 0.5 | 1 | $VUMAT_{0.5\text{-}0.5\text{-}1}$ |
| | 0.57 | 0.57 | 1 | $VUMAT_{0.57\text{-}0.57\text{-}1}$ |
| Crushable Foam (CF) | 1 | 0.5 | 3 | $CF_{1\text{-}0.5\text{-}3}$ |
| | | | 2 | $CF_{1\text{-}0.5\text{-}2}$ |
| | | | 1.5 | $CF_{1\text{-}0.5\text{-}1.5}$ |
| | | | 1 | $CF_{1\text{-}0.5\text{-}1}$ |
| | | | 0.75 | $CF_{1\text{-}0.5\text{-}0.75}$ |
| | 1 | 0.75 | 3 | $CF_{1\text{-}0.75\text{-}3}$ |
| | | | 2 | $CF_{1\text{-}0.75\text{-}2}$ |
| | | | 1.5 | $CF_{1\text{-}0.75\text{-}1.5}$ |
| | | | 1 | $CF_{1\text{-}0.75\text{-}1}$ |
| | | | 0.75 | $CF_{1\text{-}0.75\text{-}0.75}$ |
| | 1 | 0.68 | 1 | $CF_{1\text{-}0.68\text{-}1}$ |
| | 0.6 | 0.5 | 1 | $CF_{0.6\text{-}0.5\text{-}1}$ |
| | 0.5 | 0.5 | 1 | $CF_{0.5\text{-}0.5\text{-}1}$ |
| | 0.57 | 0.57 | 1 | $CF_{0.57\text{-}0.57\text{-}1}$ |

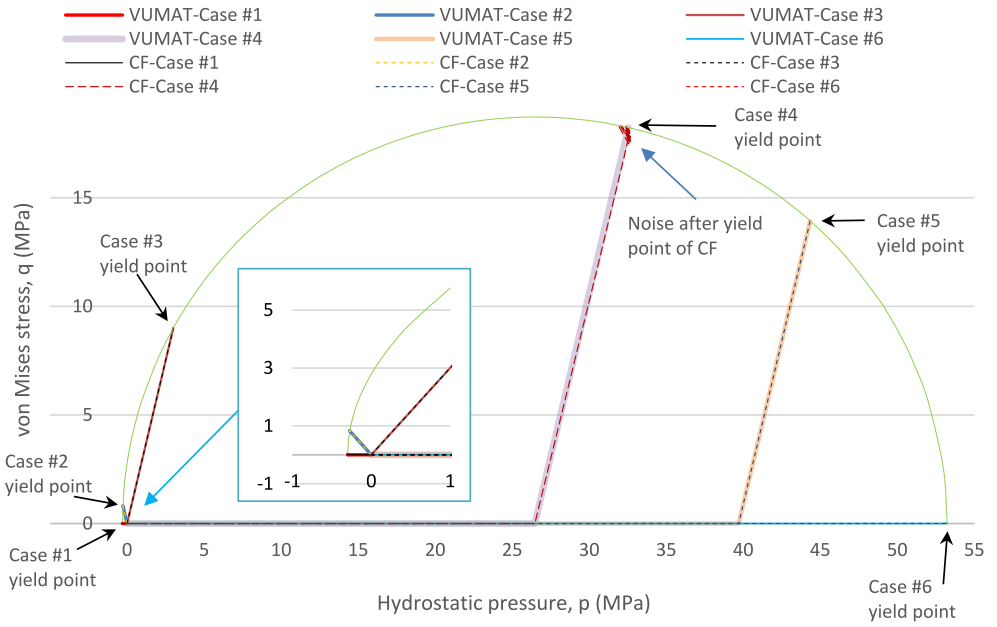


**Fig. 9.** *p-q* paths for different load cases.

the equivalent plastic strain reached the failure strain (Fig. 10), indicating that the failure model works properly. For Case #7, both plasticity models returned very similar results so that erosion occurred at $\bar{\varepsilon}^p = 0.49$ and $t = 90$–$95$ ms for both models. Conversely, they produced significantly different results for Case #8. Evidently, the confinement condition has made no noticeable difference in the results produced by the CF model while it has tremendously affected the VUMAT results. Hence, it can be concluded that the VUMAT captures confinement effects, and the CF model is confinement insensitive. This means that the CF material model (without implementing the manual discretization technique) is incapable of generating high-pressure zones caused by high confining pressures in the

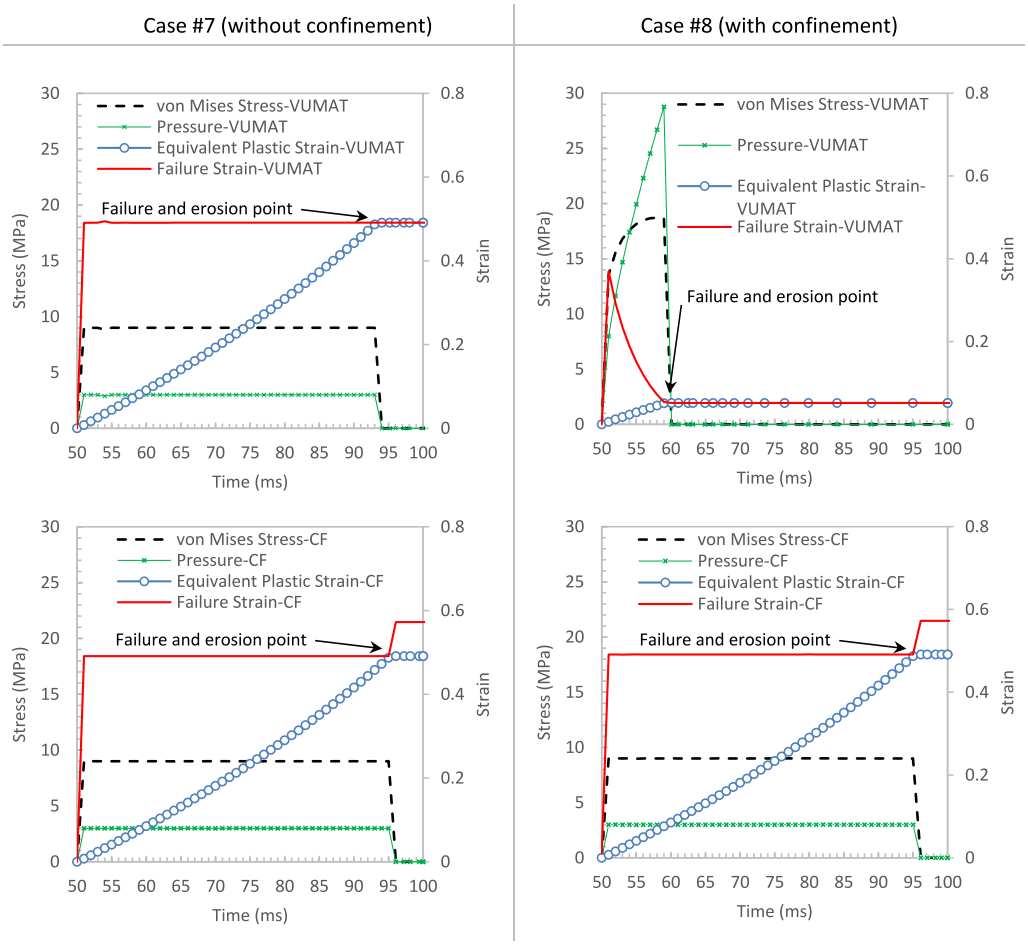


**Fig. 10.** Case #7 and Case #8 results produced by the VUMAT (top row) and the CF model (bottom row).

ice domain during crushing. This explains why the manual discretization technique for assigning high and low yield stress properties to the ice domain has been used in the crushable foam approach reported in the literature. It is simply due to the zero plastic Poisson's ratio of the CF plasticity model, which means that axial loading of an element results in almost zero transverse deformations. Zero transverse deformation causes zero interaction between the element and the confining walls (or the adjacent elements in an ice crushing simulation) no matter how large is the axial deformation.

For Case #8, the VUMAT simulates a gradual build-up of pressure in the element. This increase in pressure results in a stiffer element as the yield stress climbs up on the yield surface (see Fig. 4 for the yield surface shape). The von Mises stress history produced by the VUMAT illustrates a section of the elliptical yield envelope until the element is eroded (Fig. 10). In addition, according to Eq. (36) (graphed in Fig. 11 for $M = 1$ and $N = 0.75$), the failure strain should drop in a parabolic trend as the pressure increases until $p =$ 40.3 MPa. This parabolic fall of the failure strain is also observed in Fig. 10 for Case #8 results produced by the VUMAT so that the element is deleted at $\bar{\varepsilon}^p = 0.05$ and $t = 60$ ms. In contrast, the failure strain produced by the CF model for Case#8 remains flat at 0.49 until the element is eroded at $t = 95$ ms, the same as Case #7.

### 6.2. Cone ice crushing

#### 6.2.1. Mesh sensitivity analysis

To investigate the influence of element size on the cone ice crushing simulations, 20 simulations were carried out, and their results are discussed in this section. Fig. 12 displays the experimental and numerical *F-D* curves, where *F* is the normal contact force, and *D* is the indenter displacement. There are two significant drops in the experimental curves which is due to stopping and restarting the indentation [22]. The stops are not considered in the numerical simulations. Figs. 13 and 14 show the *P-A* curves derived from the *F-D* curves. The contact pressure, *P*, and the nominal contact area, *A*, were calculated as follows

$$P = \frac{F}{A};\ A = \pi(D\tan(60^\circ))^2 \qquad (37a;\ 37b)$$

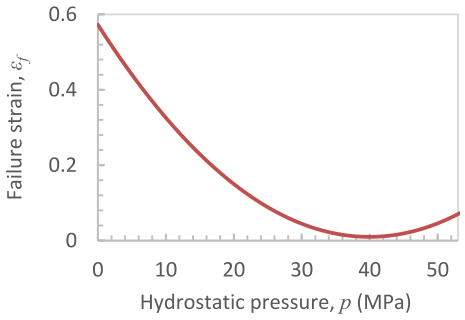


**Fig. 11.** Eq. (36) graphed for $M = 1$ and $N = 0.75$.

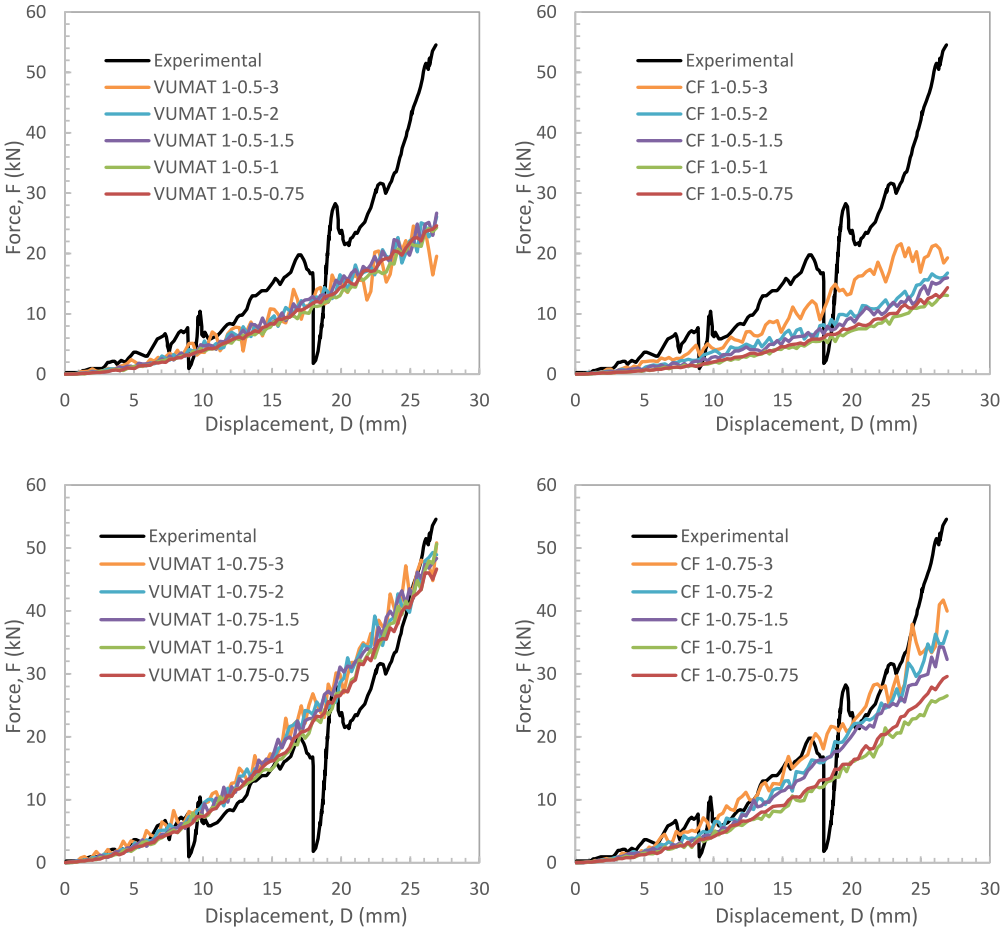


**Fig. 12.** Force vs. displacement for five different element sizes and two sets of failure strain constants.

Figs. 12–14 demonstrate that element size has a significant effect on the CF model results while the VUMAT exhibits less sensitivity to the element size. According to Figs. 13 and 14, reducing the element size from 1 to 0.75 mm, which increased the number of elements from 73844 to 176382, has not noticeably influenced the *P-A* curves in any of the displayed plots. Therefore, the element size of 1 mm was selected to generate the mesh of the cone ice models developed for the calibration study. For model names and their corresponding element size see Table 3.

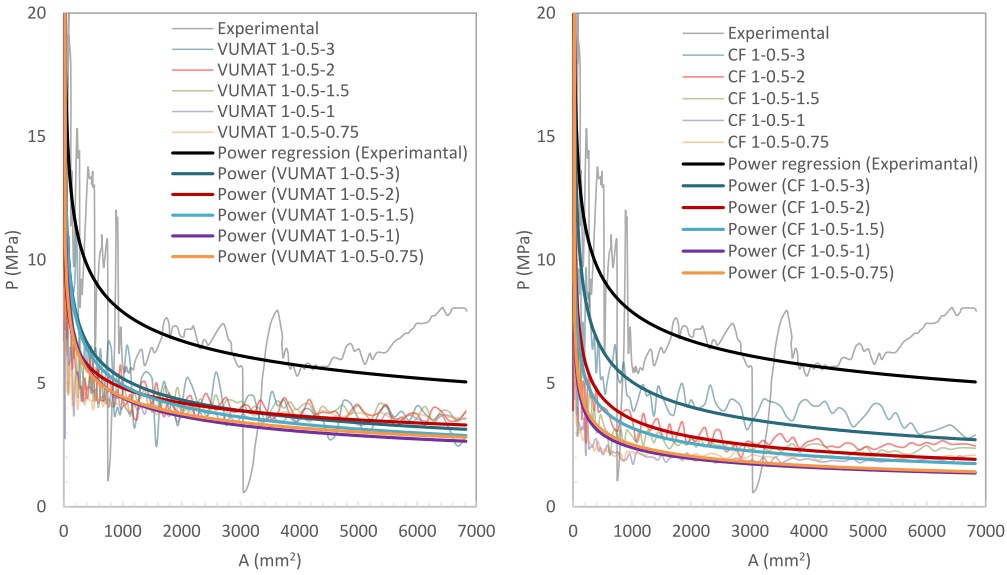


**Fig. 13.** Contact pressure vs. nominal contact area for five different element sizes ($M = 1$ and $N = 0.5$).

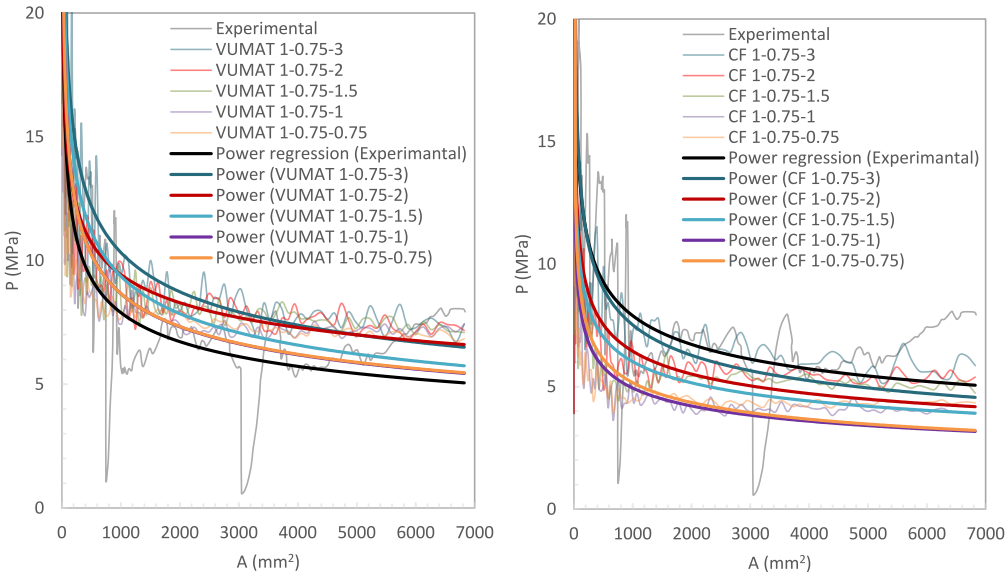


**Fig. 14.** Contact pressure vs. nominal contact area for five different element sizes ($M = 1$ and $N = 0.75$).

Figs. 12–14 show that the CF model produces much less force and contact pressure compared to the VUMAT. This is, as discussed in the previous section, caused by the zero plastic Poisson's ratio of the Crushable Foam plasticity model leading to lower confining pressure in the ice domain compared to the VUMAT simulations. According to the yield locus, for $p \leq \frac{p_c - p_t}{2}$, a larger confining pressure results in a higher yield stress. In Fig. 15, the zone of high hydrostatic pressure (reflecting high-pressure zone) is observed for the VUMAT results. In this figure, the size and magnitude of the pressure field produced by the CF model are far smaller than those produced by the VUMAT.

Fig. 16 illustrates the internal and artificial energies produced by the VUMAT and the CF model. The ratio of the artificial energy to the internal energy is higher for the VUMAT due to the larger transverse deformations in elements resulting in larger element distortions and hourglassing that need to be numerically controlled by adding artificial stiffness.

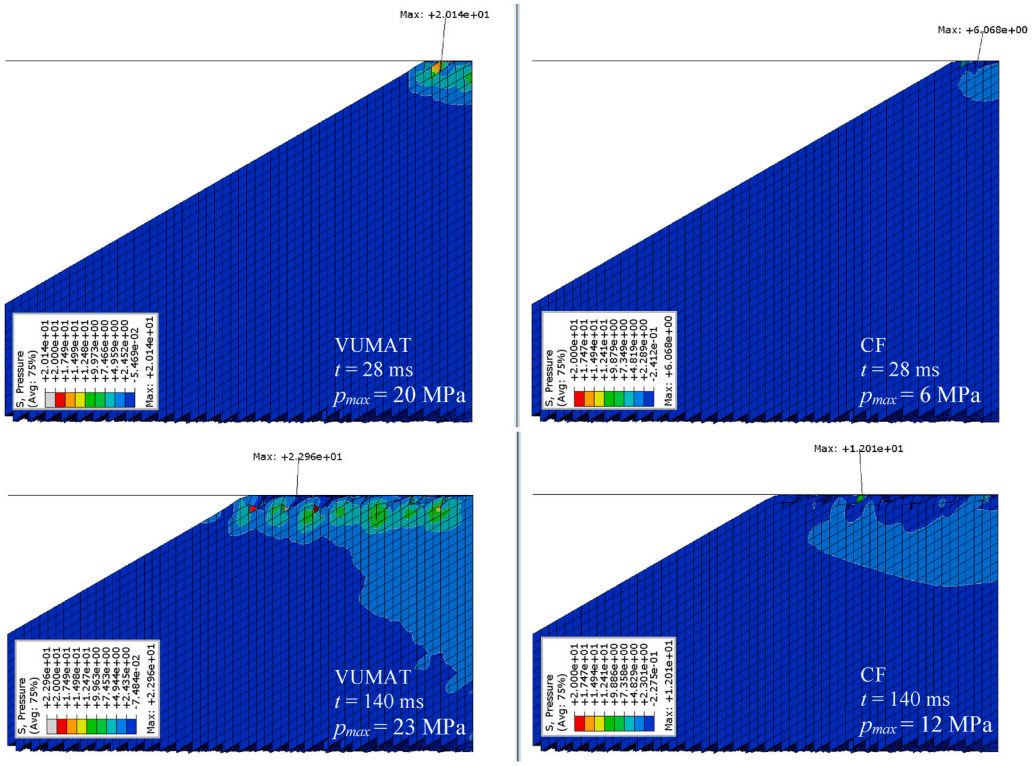


**Fig. 15.** Hydrostatic pressure distribution in the ice domain produced by the VUMAT and the CF model at different times ($M = 1$ and $N = 0.75$).

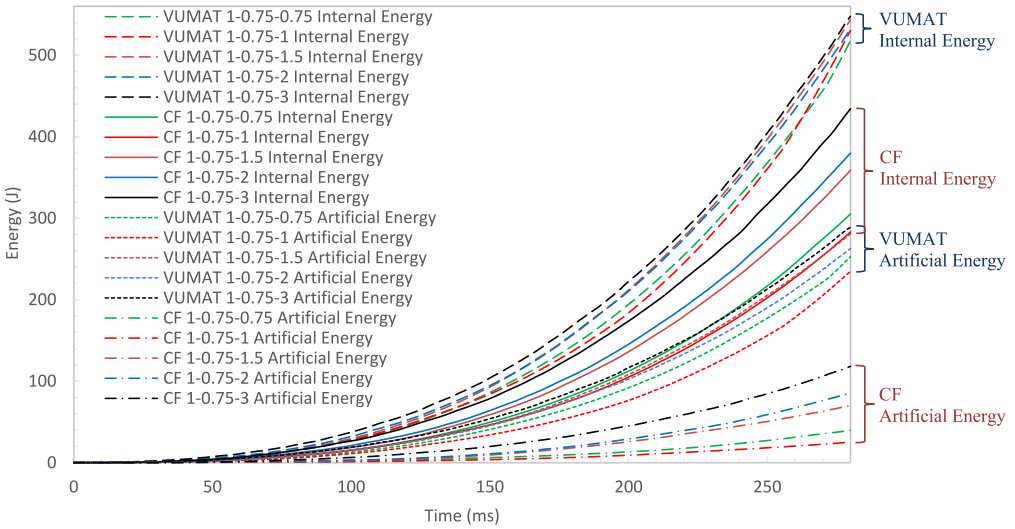


**Fig. 16.** The effects of material model and element size on the internal and artificial energies ($M = 1$ and $N = 0.75$).

### 6.2.2. *Calibration of the failure parameters*

*P-A* curves for different sets of *M* and *N* values are given in Fig. 17. The *P-A* curves from the VUMAT simulations correlate very closely with the experimental results for two sets of *M* and *N* values; 1–0.75 and 0.57–0.57. This is because they yield very similar failure strains for the pressure at which element failure occurs (see Fig. 18). The *P-A* curves produced by the CF model drop far more rapidly and bend more abruptly than those from the VUMAT. As discussed earlier this is because the Crushable Foam model fails to correctly simulate the confining pressure. The best correlation between the *P-A* curves from the CF model and the experimental one was achieved for two pairs of *M* and *N* values, 0.5–0.5 and 0.57–0.57. The pair 0.57–0.57 is the ideal choice here as it delivers the best correlation with the experimental results for both the VUMAT and the CF model.

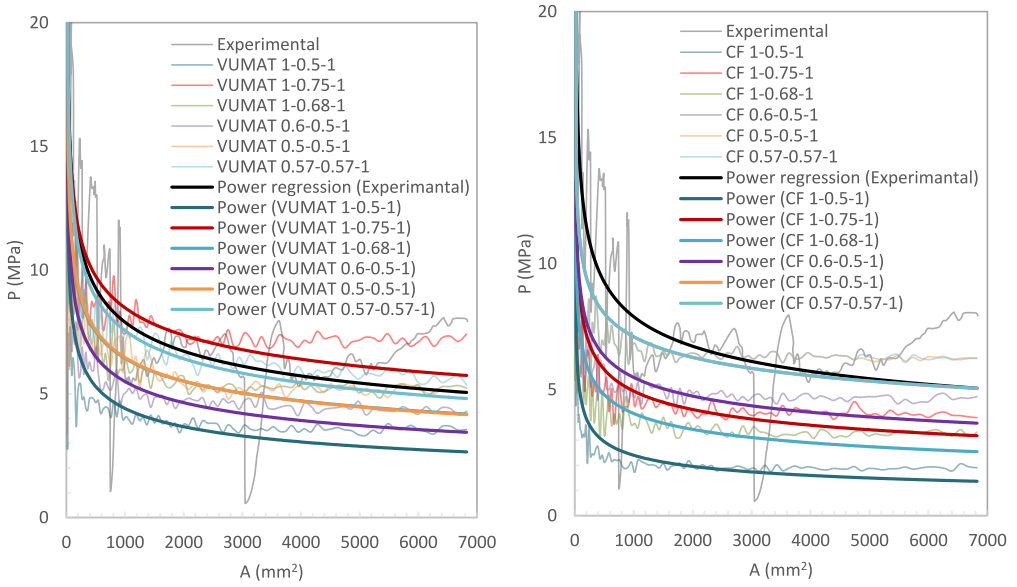


**Fig. 17.** Contact pressure vs. nominal contact area from the VUMAT and the CF model with different $M$ and $N$ values.

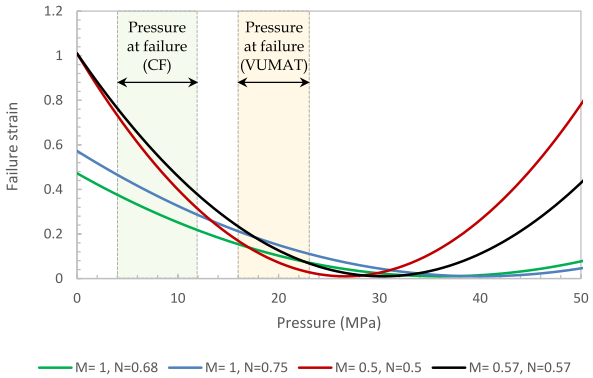


**Fig. 18.** Failure strain vs. hydrostatic pressure from Eq. (36) for different $M$ and $N$ values.

**Table 4**
*P-A* relationships for all the studied cone ice crushing cases.

| Model # | *P-A* relationship (Experimental: $P = 39.21\ A^{-0.232}$) | $R^2$ | Model # | *P-A* relationship (Experimental: $P = 39.21\ A^{-0.232}$) | $R^2$ |
|---|---|---|---|---|---|
| $VUMAT_{1\text{-}0.5\text{-}3}$ | $P = 31.99\ A^{-0.263}$ | 0.801 | $CF_{1\text{-}0.5\text{-}3}$ | $P = 47.65\ A^{-0.325}$ | 0.656 |
| $VUMAT_{1\text{-}0.5\text{-}2}$ | $P = 18.52\ A^{-0.195}$ | 0.815 | $CF_{1\text{-}0.5\text{-}2}$ | $P = 31.87\ A^{-0.318}$ | 0.741 |
| $VUMAT_{1\text{-}0.5\text{-}1.5}$ | $P = 33.99\ A^{-0.279}$ | 0.719 | $CF_{1\text{-}0.5\text{-}1.5}$ | $P = 27.87\ A^{-0.314}$ | 0.757 |
| $VUMAT_{1\text{-}0.5\text{-}1}$ | $P = 27.39\ A^{-0.264}$ | 0.655 | $CF_{1\text{-}0.5\text{-}1}$ | $P = 18.20\ A^{-0.295}$ | 0.785 |
| $VUMAT_{1\text{-}0.5\text{-}0.75}$ | $P = 23.04\ A^{-0.238}$ | 0.671 | $CF_{1\text{-}0.5\text{-}0.75}$ | $P = 20.02\ A^{-0.3}$ | 0.756 |
| $VUMAT_{1\text{-}0.75\text{-}3}$ | $P = 54.70\ A^{-0.241}$ | 0.838 | $CF_{1\text{-}0.75\text{-}3}$ | $P = 45.41\ A^{-0.26}$ | 0.531 |
| $VUMAT_{1\text{-}0.75\text{-}2}$ | $P = 34.03\ A^{-0.186}$ | 0.856 | $CF_{1\text{-}0.75\text{-}2}$ | $P = 30.59\ A^{-0.225}$ | 0.544 |
| $VUMAT_{1\text{-}0.75\text{-}1.5}$ | $P = 54.39\ A^{-0.255}$ | 0.715 | $CF_{1\text{-}0.75\text{-}1.5}$ | $P = 28.23\ A^{-0.224}$ | 0.562 |
| $VUMAT_{1\text{-}0.75\text{-}1}$ | $P = 34.39\ A^{-0.242}$ | 0.511 | $CF_{1\text{-}0.75\text{-}1}$ | $P = 24.37\ A^{-0.231}$ | 0.720 |
| $VUMAT_{1\text{-}0.75\text{-}0.75}$ | $P = 45.53\ A^{-0.24}$ | 0.752 | $CF_{1\text{-}0.75\text{-}0.75}$ | $P = 28.39\ A^{-0.247}$ | 0.723 |
| $VUMAT_{1\text{-}0.68\text{-}1}$ | $P = 30.26\ A^{-0.224}$ | 0.565 | $CF_{1\text{-}0.68\text{-}1}$ | $P = 21.84\ A^{-0.244}$ | 0.720 |
| $VUMAT_{0.6\text{-}0.5\text{-}1}$ | $P = 29.47\ A^{-0.243}$ | 0.6125 | $CF_{0.6\text{-}0.5\text{-}1}$ | $P = 23.28\ A^{-0.209}$ | 0.655 |
| $VUMAT_{0.5\text{-}0.5\text{-}1}$ | $P = 31.54\ A^{-0.229}$ | 0.573 | $CF_{0.5\text{-}0.5\text{-}1}$ | $P = 24.13\ A^{-0.177}$ | 0.565 |
| $VUMAT_{0.57\text{-}0.57\text{-}1}$ | $P = 38.40\ A^{-0.235}$ | 0.599 | $CF_{0.57\text{-}0.57\text{-}1}$ | $P = 24.16\ A^{-0.177}$ | 0.565 |

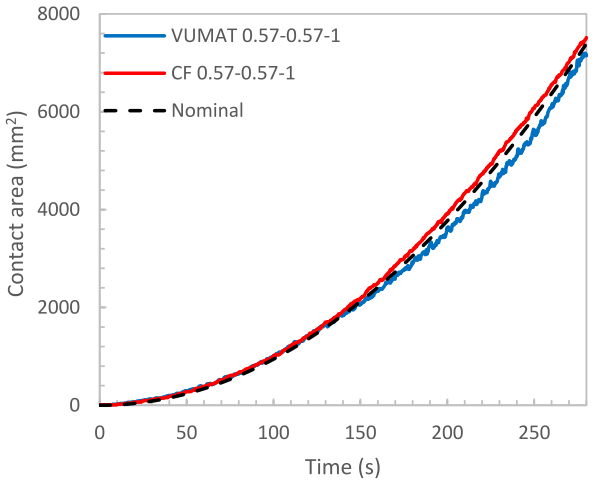


**Fig. 19.** Nominal and numerical contact area histories.

*P-A* relationships for all the studied cone ice crushing cases together with their goodness of fit in terms of the coefficient of determination, $R^2$, are given in Table 4. The *P-A* relationships obtained from the VUMAT model and the CF model for the *M-N* pair 0.57–0.57 (i.e., $VUMAT_{0.57\text{-}0.57\text{-}1}$ and $CF_{0.57\text{-}0.57\text{-}1}$) are $P = 38.40\,A^{-0.235}$ and $P = 24.16\,A^{-0.177}$, respectively. Thus, the VUMAT model is in better agreement with the experimental relationship, $P = 39.21\,A^{-0.232}$. It should be noted that $CF_{1\text{-}0.75\text{-}3}$ with $P = 45.41\,A^{-0.26}$ correlates better with the experimental *P-A* relationship compared with $CF_{0.57\text{-}0.57\text{-}1}$. However, it is a coincidentally good correlation obtained from an inaccurate finite element model before the mesh sensitivity analysis was performed. In finite element methods, it should be confirmed that the mesh provides a unique solution to the problem through a mesh sensitivity analysis. This is more important when the CF model is employed because its results were found to be significantly influenced by the element size. However, most of the ice crushing studies in the literature with the CF plasticity model have not reported a mesh sensitivity analysis.

To understand the effect of the material model on the contact area, the contact area histories obtained from $VUMAT_{0.57\text{-}0.57\text{-}1}$ and $CF_{0.57\text{-}0.57\text{-}1}$ are compared with each other and with the nominal contact area in Fig. 19. According to this figure, the contact areas obtained from the VUMAT and the CF model are almost the same and correlate closely with the nominal contact area used for calculating the *P-A* relationships in this study.

## 7. Concluding remarks

In the present study, the Crushable Foam (CF) plasticity model and an in-house VUMAT for elastic-plastic ice-crushing simulations were compared both theoretically, in terms of their constitutive laws, and numerically through single-element and cone crushing test simulations. Although the CF model and the VUMAT use the same yield surface, they produced significantly different results owing to their different flow rules and plastic Poisson's ratios. While the VUMAT plasticity model is governed by an associated flow rule, the CF model uses a non-associated flow rule with essentially zero plastic Poisson's ratio. This zero plastic Poisson's ratio was found to cause serious problems in ice crushing simulations.

Given that ice yield strength changes significantly with the confining pressure, there are often high and low strength zones in the crushing ice domain depending on the hydrostatic pressure distribution. Due to the zero Poisson's ratio, the CF model cannot capture the confining pressure. Therefore, the CF material model cannot correctly produce high-pressure and low-pressure zones in an ice crushing simulation. This finding explains why the users of the crushable foam approach have adopted a manual discretization technique to create high and low pressure zones by manually assigning high and low yield stress properties to the ice domain. Unlike the CF model, the VUMAT can simulate the confining pressure and produce a *P-A* curve that correlates very closely with the experimental results.

The CF model was far more sensitive to the element size compared to the VUMAT. Therefore, it is essential to perform mesh sensitivity analysis when the CF model is used for ice crushing simulations.

In practice, if the CF model is used, additional geometrical discretization has to be introduced to deal with the shortcomings of the confinement effect. However, there is no public information on how to do this beyond cone/pyramid shapes and laboratory scales. These geometrical limitations could impede the engineering application of this ice modelling approach.

## Declaration of competing interest

The authors declare that they have no known competing financial interests or personal relationships that could have appeared to influence the work reported in this paper.

## Acknowledgements

The financial support of the Research Council of Norway through the Centers of Excellence funding scheme, project AMOS (Grant number 223254) and the Centers for Research-based Innovation funding scheme, project CASA (Grant number 237885), at the Norwegian University of Science and Technology are acknowledged.

## References

[1] Liu Z, Amdahl J, Løset S. Plasticity based material modelling of ice and its application to ship–iceberg impacts. Cold Reg Sci Technol 2011;65:326–34.
[2] Sinha NK. Short-term rheology of polycrystalline ice. J Glaciol 1978;21:457–74.
[3] Sinha NK. Rheology of columnar-grained ice. Exp Mech 1978;18:464–70.
[4] Sinha NK. Creep model of ice for monotonically increasing stress. Cold Reg Sci Technol 1983;8:25–33.
[5] Sinha NK. Crack-enhanced creep in polycrystalline material: strain-rate sensitive strength and deformation of ice. J Mater Sci 1988;23:4415–28.
[6] Xiao J, Jordaan I. Application of damage mechanics to ice failure in compression. Cold Reg Sci Technol 1996;24:305–22.
[7] Xiao J. Damage and fracture of brittle viscoelastic solids with application to ice load models. Memorial University of Newfoundland; 1997.
[8] Jordaan IJ, Matskevitch DG, Meglis IL. Disintegration of ice under fast compressive loading. Int J Fract 1999;97:279–300.
[9] Jordaan IJ. Mechanics of ice–structure interaction. Eng Fract Mech 2001;68:1923–60.
[10] Taylor RS. Analysis of scale effect in compressive ice failure and implications for design. Memorial University of Newfoundland; 2010.
[11] O'Rourke BJ, Jordaan IJ, Taylor RS, Gürtner A. Experimental investigation of oscillation of loads in ice high-pressure zones, part 1: single indentor system. Cold Reg Sci Technol 2016;124:25–39.
[12] Schulson EM. Brittle failure of ice. Eng Fract Mech 2001;68:1839–87.
[13] Cammaert A, Wong T, Curtis D. Impact of icebergs on offshore gravity and floating platforms. 1983.
[14] Kim H, Kedward K. Experimental and numerical analysis correlation of hail ice impacting composite structures. In: 40th structures, structural dynamics, and materials conference and exhibit; 1999. p. 1366.
[15] Kim H, Kedward KT. Modeling hail ice impacts and predicting impact damage initiation in composite structures. AIAA J 2000;38:1278–88.
[16] Hallquist JO, Whirley RG. DYNA3D user's manual:(Nonlinear dynamic analysis of structures in three dimensions). 1989. Revision 5.
[17] Gagnon R, Derradji-Aouat A. First results of numerical simulations of bergy bit collisions with the CCGS terry fox icebreaker. In: Proceedings of the 18th IAHR international symposium on ice, sapporo. Japan: Citeseer: IAHR & AIRH; 2006.
[18] Gagnon R. Results of numerical simulations of growler impact tests. Cold Reg Sci Technol 2007;49:206–14.
[19] Gagnon R. Numerical rendition of ice crushing. In: 20th IAHR international symposium on ice. Citeseer; 2010. p. 14–8.
[20] Gagnon R. A numerical model of ice crushing using a foam analogue. Cold Reg Sci Technol 2011;65:335–50.
[21] Kim H. Simulation of compressive 'cone-shaped' ice specimen experiments using LS-DYNA. In: Proceedings of the 13th international LS-DYNA users conference dearborn; 2015. MI, USA.
[22] Kim H, Daley C, Colbourne B. A numerical model for ice crushing on concave surfaces. Ocean Eng 2015;106:289–97.
[23] Kim H, Quinton B. Evaluation of moving ice loads on an elastic plate. Mar Struct 2016;50:127–42.
[24] Kim J-H, Kim Y. Numerical simulation of concrete abrasion induced by unbreakable ice floes. Int J Nav Archit Ocean Eng 2019;11:59–69.
[25] Obisesan A, Sriramula S. Efficient response modelling for performance characterisation and risk assessment of ship-iceberg collisions. Appl Ocean Res 2018;74:127–41.
[26] Price A, Quinton BW, Veitch B. Shared-energy prediction model for ship-ice interactions. OnePetro: SNAME Maritime Convention; 2021.
[27] Gagnon R, Wang J. Numerical simulations of a tanker collision with a bergy bit incorporating hydrodynamics, a validated ice model and damage to the vessel. Cold Reg Sci Technol 2012;81:26–35.
[28] Cao B, Bae D-M, Sohn J-M, Prabowo AR, Chen TH, Li H. Numerical analysis for damage characteristics caused by ice collision on side structure. In: International conference on offshore mechanics and arctic engineering. American Society of Mechanical Engineers; 2016. V008T07A19.
[29] Wang B, Yu H-C, Basu R. Ship and ice collision modeling and strength evaluation of LNG ship structure. In: International conference on offshore mechanics and arctic engineering; 2008. p. 911–8.
[30] Han D, Lee H, Choung J, Kim H, Daley C. Cone ice crushing tests and simulations associated with various yield and fracture criteria. Ships Offshore Struct 2017;12:S88–99.
[31] ISO19906 I. Petroleum and natural gas industries–arctic offshore structures. Geneva: ISO; 2010.
[32] Kim E, Storheim M, von Bock und, Polach R, Amdahl J. Design and modelling of accidental ship collisions with ice masses at laboratory-scale. In: International conference on offshore mechanics and arctic engineering. American Society of Mechanical Engineers; 2012. p. 495–505.
[33] Kim E. Experimental and numerical studies related to the coupled behavior of ice mass and steel structures during accidental collisions. 2014.
[34] Song M, Kim E, Amdahl J, Ma J, Huang Y. A comparative analysis of the fluid-structure interaction method and the constant added mass method for ice-structure collisions. Mar Struct 2016;49:58–75.
[35] Lu W, Yu Z, Berg Mvd, Monteban D, Lubbad R, Hornnes V, et al. Loads, design and operations of floaters in the arctic (nord ST20). In: PTIL - LASTER, DESIGN OG OPERASJON AV FLYTERE I NORDOMRÅDENE (NORD ST20) 2019/313; 2019.
[36] Wang X. Analysis of iceberg-structure interaction during impacts. NTNU; 2020.
[37] Yu Z, Amdahl J. A numerical solver for coupled dynamic simulation of glacial ice impacts considering hydrodynamic-ice-structure interaction. Ocean Eng 2021;226:108827.
[38] Derradji-Aouat A. A unified failure envelope for isotropic fresh water ice and iceberg ice. In: Proceedings of ETCE/OMAE Joint Conference Energy for the New Millenium; 2000.
[39] Gagnon R, Gammon P. Triaxial experiments on iceberg and glacier ice. J Glaciol 1995;41:528–40.
[40] Tsai SW, Wu EM. A general theory of strength for anisotropic materials. J Compos Mater 1971;5:58–80.
[41] Mánik T. A natural vector/matrix notation applied in an efficient and robust return-mapping algorithm for advanced yield functions. Eur J Mech Solid 2021;90:104357.
[42] Huang J, Griffiths D. Return mapping algorithms and stress predictors for failure analysis in geomechanics. J Eng Mech 2009;135:276–84.
[43] Abedrabbo N, Pourboghrat F, Carsley J. Forming of aluminum alloys at elevated temperatures – Part 2: numerical modeling and experimental verification. Int J Plast 2006;22:342–73.
[44] ABAQUS standard user's manual. Version 6.14. Providence, RI, USA: Dassault Systemes Simulia Corp; 2014.
[45] Hallquist J. LS-dyna keyword user's manual. Livermore, California, USA: Livermore Software Technology Corporation (LSTC); 2006.
[46] Mavrodontis N. Abaqus Hardening Laws on single element model. Simuleon; 2020. https://info.simuleon.com/blog/abaqus-hardening-laws-on-single-element-model.
[47] Kierkegaard H. Ship collisions with icebergs: Danmarks Tekniske Højskole. Instituttet for Skibs-og Havteknik; 1993.